Published in final edited form as:
Adv Funct Mater. 2014 April 16; 24(15): 2188–2196. doi:10.1002/adfm.201302901.

Arrayed Hollow Channels in Silk-based Scaffolds Provide Functional Outcomes for Engineering Critically-sized Tissue Constructs

Dr Jelena Rnjak-Kovacina[‡], **Lindsay S. Wray**[‡], **Julianne M. Golinski**, and **Prof David L. Kaplan**[*]
Department of Biomedical Engineering, Science and Technology Centre, 4 Colby Street, Medford MA 02155, USA

Abstract

In the field of regenerative medicine there is a need for scaffolds that support large, critically-sized tissue formation. Major limitations in reaching this goal are the delivery of oxygen and nutrients throughout the bulk of the engineered tissue as well as host tissue integration and vascularization upon implantation. To address these limitations we previously reported the development of a porous scaffold platform made from biodegradable silk protein that contains an array of vascular-like structures that extend through the bulk of the scaffold. Here we report that the hollow channels play a pivotal role in enhancing cell infiltration, delivering oxygen and nutrients to the scaffold bulk, and promoting *in vivo* host tissue integration and vascularization. The unique features of this protein biomaterial system, including the vascular structures and tunable material properties, render this scaffold a robust and versatile tool for implementation in a variety of tissue engineering, regenerative medicine and disease modeling applications.

Keywords

silk; tissue engineering; oxygen/nutrient delivery; vascularization; porous scaffolds

1. Introduction

Three-dimensional (3D), bioengineered tissues offer promise for the replacement and regeneration of injured or diseased organs as well as for *in vitro* modeling of human disease states and drug treatment regimes. Analogues of a range of tissues, including skin, bone, ligament, adipose, muscle, liver and kidney among others, have been developed *in vitro*, typically using polymer scaffolds populated with appropriate cell types. However, the size of these constructs is generally limited to several hundred micrometers due to restrictions in achieving homogenous cell distribution and exchange of nutrients, gases and waste in larger constructs. This problem persists *in vivo* where large constructs display poor host tissue integration and vascularization.[1] To overcome oxygen and nutrient delivery limitations in regenerating tissues, attempts have been made to direct and expedite the vascularization

david.kaplan@tufts.edu.
‡Authors contributed equally to this work

process using approaches that include angiogenic growth factor delivery, *in vitro* and *in vivo* pre-vascularization and use of vascular-inductive biomaterials.[2-5] However, on their own these approaches have demonstrated limited clinical success and the future outlook for vascularization strategies will likely involve a coordinated combination of these individual strategies.[4] To this end, attempts are being made to develop tissue engineering platforms that augment traditional vascularization approaches for supporting large tissue formation and regeneration. These attempts take a direct approach toward rapid vascularization of tissue constructs by engineering vascular-like conduits into the scaffold.[6-11]

A promising approach employs microfabrication techniques, such as soft lithography, sacrificial molding, and modular assembly, to build conduits that mimic the structural hierarchy of blood vessels.[6, 7, 12] The effectiveness of these technologies in vascularizing engineered tissues has recently been demonstrated in a mouse model in which the vascular conduits supported *in vitro* pre-capillary formation and upon implantation anastomosed with the host vasculature.[13] These techniques, however, result in constructs that are inherently limited to thin (<1 mm) units. To build larger 3D constructs these units must be bonded together and precisely assembled to ensure alignment of the vascular conduits.[7, 14] The process of stacking the layers has been demonstrated in the literature and is therefore physically feasible but the question of practicality still needs to be addressed.

In contrast, methods for building monolithic tissue constructs that contain vascular conduits without the need for multi-layer assembly will be advantageous in terms of ease of experimentation and clinical implementation. A number of techniques have been developed to generate vascular-like structures within monolithic, 3D tissue constructs, including casting scaffolds around stainless steel wires[15, 16], laser piercing channels[8, 10] and use of sacrificial molding.[9, 17, 18] These previous reports, however, are limited with regard to fabrication efficiency and versatility, biocompatibility and biodegradation properties of scaffolding materials, scaffold porosity, and demonstrated tissue formation and functionality.

Here we report on a tissue construct platform that contains an array of hollow channels in a porous, silk protein scaffold that is capable of supporting large tissue formation. Previously we demonstrated the use a unique linear wire array that efficiently and reproducibly builds small diameter channels through the bulk of large (i.e. scaffold dimensions greater than 500 μm) scaffolds and we showed the highly tunable material properties of the resulting platform.[11] The versatility of this platform stems from the unique linear wire arrays and the use of silk, a cytocompatible, biodegradable protein polymer with highly tunable physical and biological properties. In addition to controllable mechanical and biodegradation properties, silk has been demonstrated to support stabilization and controlled delivery of a range of biological molecules thereby expanding its versatility in engineering tissues.[19]

In the present study we report that the hollow channel arrays play a crucial role in enhancing cell infiltration, oxygen and nutrient delivery to the bulk of engineered tissues, and promoting *in vivo* scaffold integration and vascularization. These findings are significant in that they explicitly overcome the primary obstacles to building or regenerating large, complex tissues. This technology has potential to advance the state-of-the-art in the tissue

engineering field toward the development of relevant tissue constructs for regenerative medicine and tissue modeling purposes.

2. Results

2.1. Hollow channels improve cell infiltration and distribution in critically-sized scaffolds *in vitro*

Cells were seeded on both surfaces of large silk scaffolds (12 mm ø, 15 mm height) in the presence or absence of an array of 508 μm hollow channels and distribution of live (calcein AM stained) cells was imaged along the scaffold length **(Figure 1a)**. Hollow channels improved cell infiltration into the scaffold, resulting in even distribution of cells throughout the construct length, while scaffolds without the hollow channels displayed areas with limited cell infiltration in the middle of the construct **(Figure 1b)**. The extent of cell infiltration was quantified by measuring the gray value of green pixels along the scaffold cross-section **(Figure 1c)**. This image analysis revealed that more cells infiltrated the channeled scaffolds, compared to unchanneled scaffolds **(Figure 1d)**. Interestingly, in the unchanneled scaffolds, more cells were observed on the scaffold surface, forming a dense cell crust compared to the channeled scaffold **(Figure 1e)**.

2.2 Hollow channels help overcome oxygen and nutrient delivery limitations

To investigate the effect of the channels on oxygen diffusion into the tissue construct, cells were seeded in large silk scaffolds (12 mm ø, 4 mm height) in the presence and absence of an array of 508 μm diameter hollow channels. Cells were seeded into the bulk of the scaffold with a fibrin hydrogel. To ensure that hollow channels remained clear of the cells and hydrogel, cell seeding was performed in the presence of the LWA, which was removed following fibrin gelation **(Figure 2a)**. Oxygen saturation through the middle of the scaffold was determined at five positions along the center axis, from the scaffold edge inwards (Figure 2a). In addition to oxygen saturation, live cell distribution and cell metabolism were monitored to account for differences in cell number and distribution. No difference in cell metabolism **(Figure 2b)** and cell distribution **(Figure 2c and Figure S1 a-c)** were observed between channeled and unchanneled constructs over a 28-day period under static culture conditions. Acellular scaffolds maintained in cell culture media under standard 20% oxygen cell culture conditions displayed ~20% oxygen saturation (19.1 ± 1.5% and 19.4 ± 1.5% in the absence and presence of hollow channels respectively). At day seven post-seeding, higher ($p<0.05$) oxygen saturation was recorded in channeled constructs compared to unchanneled constructs in the middle of the construct (5 and 6 mm from the edge), while at day 28 higher oxygen saturation was recorded along the scaffold width in the channeled constructs ($p<0.01$ at 2 mm and $p<0.05$ at 3-6 mm) **(Figure 2d)**. Overall, channeled scaffolds displayed significantly higher average oxygen saturation compared to unchanneled scaffolds at both day seven (12.1 ± 3.4% vs 6.4 ± 3.0%) and day 28 (9.7% ± 3.0% vs 3.8 ± 1.2%) **(Figure S1d)**.

The effect of channels on oxygen diffusion in the tissue construct under perfusion culture was also investigated at day seven post-seeding. No difference in cell distribution was observed in channeled compared to unchanneled scaffolds, but more cells were observed

under perfusion culture compared to static culture **(Figure 2e and Figure S2 a-c)**. Under perfusion culture, the presence of channels improved oxygen saturation along the width of the construct ($p<0.05$ and $p<0.01$) **(Figure 2f)**, from 7.8 ± 3.4% average oxygen saturation in unchanneled constructs to 14.1 ± 1.7% average oxygen saturation in channeled constructs ($p<0.01$) **(Figure S2d)**.

Nutrient delivery to cellular silk constructs was modeled by imaging calcein AM (fluoresces green once processed by living cells) diffusion into large, cell-seeded silk constructs (12 mm ø, 6 mm height). At day 1 post-seeding, constructs were incubated with calcein AM, either before (experimental, post-cut) or after (control, pre-cut) slicing along the scaffold midline **(Figure 3a)**. Pre-cut control samples confirmed the presence of live cells in the middle of both channeled and unchanneled constructs **(Figure 3b)**, while the post-cut experimental constructs modeled calcein AM diffusion into the scaffold to reach cells in the middle of the construct. After 45 min of calcein AM incubation, calcein AM fluorescence was not observed in the unchanneled scaffolds, indicating that calcein AM diffusion to the middle of the scaffold was considerably limited. In contrast, calcein AM fluorescence was observed surrounding the channels with an average maximum diffusion distance of 321.7±13.5 radius **(Figure 3c)**, indicating improved calcein AM diffusion in channeled constructs.

2.3 Hollow channels improve scaffold integration *in vivo*

Acellular unchanneled and channeled (254 μm and 508 μm ø channels) silk scaffolds (8 mm ø, 2 mm height) were implanted subcutaneously in mice and examined at weeks two and four post-implantation for construct integration and vascularization using histological techniques. Silk scaffolds elicited a typical host immune response upon implantation, with no severe negative inflammatory response. Explanted scaffolds were sectioned in two orientations: ‘side view’ and ‘top view’ **(Figure 4a)**. The presence of hollow channels, regardless of channel diameter improved cell infiltration into silk scaffolds **(Figure 4b)** as measured from cellular areas in H&E stained scaffold sections. Cell infiltration into silk scaffolds was observed in side view cross-sections starting at both scaffold surfaces and proceeding inwards **(Figure 4c)**. At week two, immune cells were observed in all constructs, but by week four the predominant cell type was dermal fibroblasts. The infiltrating cell front was observed at each channel cross-section in 254 μm- and 508 μm- diameter channeled scaffolds at week two and the hollow channels were mostly filled with infiltrating cells by week four (Figure 4c). In the top view of channeled scaffolds at week four, dense areas of infiltrated cells were observed in 254 μm scaffolds, with diameters spanning over 1 mm in some areas, diameters much larger than the original hollow channels **(Figure 4d)**. This indicates that cell infiltrated through the hollow channels and radiated outwards into the scaffold bulk. In 508 μm scaffolds, cell areas infiltrating through the channels connected to one another (Figure 4d).

At week two, both the 254 μm diameter and 508 μm diameter channeled explants displayed a higher level of vascularization compared to unchanneled scaffolds, as indicated by red coloring of the constructs and better attachment to the mouse subdermis **(Figure 5a)**. Masson’s trichrome stain of scaffold cross-sections showed scaffold remodeling by infiltrating fibroblasts, which deposited collagen (blue) in scaffold areas with high cell

density **(Figure 5b)**. Areas of high blood vessel density were observed wherever infiltrating fibroblast cells were present, which was more prominent in channeled, compared to unchanneled scaffolds (Figure 5b). The infiltrating blood vessels appeared to be functional, as they were perfused with red blood cells (Figure 5b) and the lumen wall stained positively for CD31 and α-SMA, indicating mature and patent blood vessels **(Figure 5c)**.

3. Discussion

To advance tissue engineering and regenerative medicine therapeutics to the clinic, it is imperative that technologies are developed to improve cell infiltration, oxygen and nutrient delivery and vascularization of critically-sized engineered tissues. We report on a silk-based scaffolding platform that addresses this issue using an array of hollow channels spanning the construct **(Figure 6)**.

Achieving high density and homogeneous cell distribution throughout large porous scaffolds is challenging and a range of scaffold processing techniques have been developed to increase scaffold porosity, pore size and pore interconnectivity. The work presented here shows that introduction of an array of vertical, hollow channels into lyophilized silk scaffolds is a simple and efficient means of significantly improving cell seeding into large (12 mm ø, 15 mm height) scaffolds. An array of 500 μm diameter channels, spaced 1 mm apart significantly improved delivery of cells into the scaffold bulk, resulting in a higher cell density that was more evenly distributed throughout the scaffold compared to the unchanneled silk scaffolds (Figure 1).

Inadequate delivery of oxygen and nutrients to and clearing of waste products from cells is the primary obstacle in engineering physiologically relevant, critically-sized tissue equivalents for both *in vitro* tissue modeling and *in vivo* tissue replacement. Tissue equivalents thicker than several hundred microns fail to integrate *in vivo* and are prone to necrosis at the core of the construct, which can stimulate undesirable inflammatory responses in the body.[2, 5] Techniques have been developed to address this problem, including delivery of oxygen carriers (eg. perfluorocarbon), delivery of vascularization promoting factors such as VEGF and *in vitro* construct vascularization with endothelial cells.[3] While these techniques have been successful for small, simple tissue constructs, it has yet to be shown whether these techniques can provide the necessary oxygen and nutrient delivery to large tissue constructs in a fashion that is efficient and clinically relevant. Introduction of an array of hollow channels into silk scaffolds is a simple, efficient, and reproducible means of addressing oxygen and nutrient delivery limitations in critically-sized constructs. We demonstrate that the presence of an array of 500 μm diameter channels with 1 mm spacing increases the amount of oxygen delivered to cell-seeded constructs by 1.9-fold at day seven and 2.6-fold at day 28 compared to unchanneled constructs when seeded under static conditions (Figure 2b-d and Figure S1). Decreased oxygen saturation in both channeled and unchanneled constructs at day 28 compared to day seven is likely the result of increased cellular density and therefore higher oxygen demand by the constructs. However, it is interesting to note that even though there were no differences in cellular density and distribution between channeled and unchanneled constructs at day 28, the oxygen saturation

in channeled scaffolds at day 28 was higher than in unchanneled scaffolds at day seven, pointing to the utility of hollow channels in efficiently delivering oxygen to cells.

When cultured under perfusion conditions, channeled scaffolds displayed higher oxygen saturation than unchanneled scaffolds, but the extent of the difference was less than under static conditions (3.0-fold difference under static, 1.8-fold difference under perfusion conditions) (Figure 2e-f and Figure S2). Even though perfusion culture resulted in higher cell density and therefore higher oxygen demand, overall oxygen saturation was higher in perfusion cultures compared to static in both channeled and unchanneled scaffolds. These data point to the complementary properties of perfusion culture and channels in delivering oxygen to critically-sized tissue equivalents.

Nutrient delivery to channeled and unchanneled constructs was modeled using calcein AM diffusion. Calcein AM is the acetomethoxy derivate of calcein, which when transported into cells fluoresces green as a result of acetomethoxy group removal by intracellular esterases.[20] This molecule is valuable in modeling nutrient delivery to cells as it is only fluorescent once inside live cells. An array of 508 μm diameter, 1 mm spaced channels enhanced calcein AM diffusion into critically-sized constructs (Figure 3) and suggests that glucose and other nutrients will be more accessible to cells at the core of critically-sized constructs with the presence of hollow channels.

When critically-sized scaffolds or bioengineered tissue equivalents are implanted *in vivo*, construct vascularization often does not occur within a sufficient time frame to ensure construct integration and remodeling.[2, 5] We demonstrate here that an array of either 254 μm- or 508 μm- diameter hollow channels spaced 1 mm apart is sufficient to significantly improve cell infiltration into acellular silk scaffolds implanted subcutaneously in mice (Figure 4). The hollow channels were the source of the improved infiltration as evidenced by large dense cell areas corresponding to channel position (Figure 4c). These dense cell areas had larger diameters compared to original channels, indicating that host tissue could migrate into the scaffold from the hollow channel space. This was particularly obvious in 508 μm diameter channels, where the cell fronts infiltrating along the channel length joined each other (Figure 4c). By week four post-implantation, the predominant cell type infiltrating into silk scaffolds were dermal fibroblasts, as evidenced by collagen deposition (Figure 5b). Fibroblast infiltration into silk scaffolds was accompanied by high-density vascularization, as the areas of high cell infiltration also displayed a high density of small-diameter blood vessels. These vessels appeared functional, as they were consistently perfused with red blood cells and expressed CD31 and α-SMA, markers of functional, mature blood vessels (Figure 5c-d). The likely mechanism of scaffold vascularization is by angiogenesis from existing vessels, but future studies involving scaffold pre-vascularization with endothelial cells and live imaging of perfused vessels will offer more insight into the specific mechanisms involved in this process. Moreover, we expect that pre-endothelialization of the hollow channels prior to implantation will further improve construct integration and vascularization. A combination of endothelial and stromal cells is known to support stable vascular network formation following implantation *in vivo*[21-23] and arranging endothelial cells into vessel-like structures is expected to accelerate anastomosis to host vasculature, as recently demonstrated by Baranski et al using microtissue molding approaches.[13] We

expect that the presence of hollow channels and accelerated cell inflitration to impact the degradation of implanted constructs. Silk degradation is directly related to crystalline content, where higher β-sheet content correlates with slower degradation[24]. In the present study we explored the effect of hollow channels on scaffold integration and implanted silk with a high β-sheet content (>45%), to exclude degradation as a signficant contributor to the outcomes. These scaffolds can be tuned to encourage rapid (days) to slow (years) degradation based on processing to control β-sheet content, which would be a useful variable to study in future work where tissue integration and regeneration are goals.

In the present study scaffolds with dimensions greater than several millimeters were assembled with a process that involved freezing and lyophilization of the silk protein solution. Lyophilized silk scaffolds are a promising biomaterials platform for engineering a range of tissue equivalents due to their highly tunable physical and biological properties, including control over pore size, pore morphology and porosity, mechanical features, degradation rates, and ease of functionalization with bioactive compounds.[11, 19] These silk scaffolds can be utilized in lieu of other currently available lyophilized biomaterial constructs, including those prepared from synthetically-derived degradable polymeric materials, such as poly(lactic-co-glycolic acid), or naturally-derived materials such as collagen and chitosan. Lyophilized silk scaffolds are assembled using an all-aqueous process, making them amenable to functionalization with bioactive agents such as extracellular matrix proteins and chemokines, without loss of function and with the benefit of stabilization. Further, lyophilized silk scaffolds do not require any chemical cross-linking to confer stabilization, mechanical strength and resistance to rapid degradation, and these systems can be designed to function *in vivo* for days to years depending on the mode of processing. [24-26]

We report the effectiveness of a simple hollow channel array within a lyophilized silk scaffold for improving cell seeding efficiency, oxygen and nutrient delivery and integration and vascularization of critically-sized silk constructs. Detailed modeling of optimal channel size and arrangement will further improve the utility of this platform for development of critically-sized tissue equivalents for tissue modeling and regenerative medicine purposes. Further, while the proof of principle was demonstrated in lyophilized silk scaffolds, this technology can be compatible with a range of other silk-based material formats, such as salt-leached sponges and gels, as well as other polymer and protein systems, making it a highly versatile platform for a range of biomedical engineering purposes.

The future outlook for vascularization of engineered tissue constructs will likely involve a coordinated combination of a variety of vascular promoting techniques including angiogenic growth factor delivery, cell delivery, and vascular inductive biomaterials.[4] Hollow channeled silk scaffolds are a promising platform for integrating these vascularization strategies in a single construct. Silk has been widely investigated in the vascular field, both as a vascular graft [27, 28] and in supporting vascular-promoting cell types including mesenchymal stem cells and endothelial cells.[11, 29] Silk materials have been extensively used for stabilization and controlled delivery of a range of biological molecules,[19] including slow release of VEGF and promotion of angiogenesis by silk hydrogels.[30] Hollow channeled scaffolds offer unique control over cell and growth factor presentation

both through the use of cell compartmentalization and silk walls surrounding the hollow channels, as we demonstrated previously.[11] This illustrates the utility of this silk-based hollow channel platform for providing a promising means for addressing the clinical need for holistic vascularization strategies for engineered tissue constructs.

4. Conclusion

Porous silk scaffolds with arrayed hollow channels exhibit favorable characteristics for engineering large tissue constructs. Arrayed hollow channels overcome significant cell infiltration, oxygen/nutrient delivery, and host tissue integration limitations, which typically hinder large tissue construct engineering. Additionally, the channel fabrication methodology is simple, reproducible and highly tunable. Channeled silk scaffolds can therefore serve as a promising off-the shelf product for a range of regenerative medicine applications including treatment of critically-size defects and provide a versatile platform for engineering three-dimensional tissues *in vitro*.

5. Experimental Section

Silk solution preparation

Silk fibroin solution was prepared as reported previously.[31] Briefly, pure silk fibroin was extracted from *Bombyx mori* cocoons by degumming the fibers in a sodium carbonate solution (0.02 M) (Sigma-Aldrich, St. Louis, MO). The pure silk fibroin was solubilized in aqueous lithium bromide (9.3 M) (Sigma-Aldrich, St. Louis, MO) at 60°C. The solution was dialyzed using Slyde-A-Lyzer Dialysis Cassettes (3500 MWCO, Thermo Scientific, Rockford, IL) against deionized water until the conductivity of the dialysis water was <10 μS cm^{-1} (indicative of complete lithium bromide removal). The concentration of the silk solution was determined by drying a know volume of the solution and massing the remaining solids. This protocol resulted in a 6-8% wt v^{-1} silk solution. Silk solutions were stored at 4°C.

Scaffold assembly

Scaffolds were prepared according to previously reported methods.[11] Briefly, linear wire arrays (LWAs) were built with either 254 μm or 508 μm diameter wires (McMaster-Carr, Elmhurst, IL) arranged into a grid pattern with 1 mm spacing between the wires. The wires were secured in place by curing polydimethylsiloxane (PDMS) around the base of the wires and placed into cylindrical molds (15 mm ø, 20 mm height). Silk solution (2-4% wt v^{-1}) was dispensed into the cylindrical molds, frozen at −20°C overnight and lyophilized, resulting in a porous scaffold. The scaffold was made insoluble by autoclaving at 121°C for 20 min to induce β-sheet formation. Scaffolds were rehydrated in water overnight. Using a biopsy punch, scaffolds were trimmed to 12 mm in diameter for *in vitro* studies and 8 mm in diameter for *in vivo* studies. Upon removal from the LWA, the height of the scaffold was trimmed using a surgical blade and a trimming device that positioned the height of the blade to the desired scaffold thickness. Scaffolds without channels were prepared in the same manner, but in the absence of the LWA.

Cell culture and scaffold seeding

Human dermal neonatal fibroblasts (hDNFs) obtained from Lonza (Basel, Switzerland) were cultured in Dulbecco's Modified Eagle Medium (supplemented with 10% fetal bovine serum, 1% antibiotic/antimycotic) (Life Technologies, Grand Island, NY) and seeded at passage 5-8. For infiltration studies, the LWA was removed prior to cell seeding; in all other experiments, the channeled scaffolds were seeded with the LWA in place as previously described.[11] LWA was removed 24 hours after cell seeding. Cells were seeded at $5\text{-}6\times10^3$ cells mm^3 in a volume of fibrin that filled the entire void space of the scaffold. Fibrin was prepared by mixing human fibrinogen (10 mg mL^{-1}) (EMD Millipore Chemicals, Billerica, MA) with human thrombin (5 U mL^{-1}) (Sigma-Aldrich, St. Louis, MO) in a 4:1 volume ratio. Cellular constructs were maintained at 37°C, 5% CO_2 in fibroblast media supplemented with aminocaproic acid (2 mg ml^{-1}) (Sigma-Aldrich, St. Louis, MO) to inhibit rapid fibrin degradation with media changes every 2-3 days. For perfusion culture, samples were cultured statically for two days and placed into a perfusion bioreactor previously designed and tested in the lab.[32] Four samples were placed into each bioreactor with media (60 mL). The rate of media perfusion through each sample was 18 μL min^{-1}. Perfusion culture was carried out for four days with a media change on the second day.

Metabolic activity

The relative number of metabolically active cells within each scaffold was determined by the AlamarBlue™ (Life Technologies, Grand Island, NY) assay according to the manufacturer's instructions. Scaffolds were washed with Phosphate Buffered Saline (PBS) and incubated in fibroblast medium with 10% AlamarBlue reagent for 2h at 37 C with 5% CO_2. Following incubation, aliquots (100 μL) were transferred to black 96-well plates and quantified for fluorescence intensity with a fluorescence plate reader using an excitation wavelength of 550 nm and an emission wavelength of 590 nm. Acellular scaffolds and tissue culture wells were also maintained in culture medium as above and were analyzed similarly as blank controls to adjust for background fluorescence.

Cell localization imaging with confocal laser scanning microscopy

Depending on the study, samples were sliced through the center either laterally or longitudinally with a surgical blade. A trimming device was designed in the lab to guide the blade through the middle of the scaffold. The scaffold halves were submerged in calcein AM (2 μM) for 45 minutes at 37°C to stain live cells. For diffusion measurements, scaffolds were incubated with calcein AM prior to cutting the scaffold in half. The scaffold halves were placed on a coverslip and imaged with a Leica DMIRE2 confocal laser scanning microscope (CLSM) with excitation at 488 nm and emission at 500-520 nm (Wetzlar, Germany). Cell distribution was analyzed from composite images spanning the length of the scaffold using 'Plot Profile' tool in Image J (National Institutes of Health, Bethesda, MD), which reports average gray value at each point across the image length.

Oxygen profile measurement

Oxygen measurements were taken along the length of the scaffold through the center according to previously reported methods [33]. Briefly, a needle-type oxygen microsensor

with a flat-broken tip (Presens, Regensberg, Germany) underwent a two-point calibration step according to the manufacturer's protocol. The oxygen sensor and the sample were placed into a specially designed positioning device that could precisely position the oxygen sensor within the scaffold using a micromanipulator. The tip of the probe was positioned at the very edge of the sample and this was considered the starting point. Before taking a reading, the probe was equilibrated for 30 seconds after which the oxygen percent was measured using the Microx TX3 transmitter and the manufacturer's data acquisition software (Presens, Regensberg, Germany). Readings were taken every 1 mm through the scaffold at 37°C and 5% CO_2. Readings were converted to % oxygen saturation by a multiplication with 0.2095, which takes into account the temperature and humidity of the incubator.

In vivo implantation

All procedures were conducted under animal care protocols approved by Tufts Institutional Animal Care and Use Committee. All animals used in this study were 4-6 week old BALB/c female mice (Charles River Laboratories, Wilmington, MA). The mice were distributed into three experimental groups (unchanneled, 254 μm and 508 μm channels) each with two time points (week 2 and week 4). The mice were randomly assigned to the experimental groups and silk scaffolds (8 mm ø, 2 mm height) were subcutaneously implanted in lateral subcutaneous pockets of each mouse under general anesthesia of oxygen and isoflurane. At week 2 or 4 post-surgery, animals were euthanized and the samples along with the overlaying tissue were collected for histological examination.

Histochemistry

Samples were fixed with 10% neutral buffered formalin (NBF) and embedded in paraffin following a series of xylene and graded ethanol incubations. Samples were sectioned to 6 μm thickness and deparaffinized. Sections were either stained with hematoxylin and eosin (H&E) (Sigma-Aldrich, St. Louis, MO) to visualize cell nuclei and cytoplasm or Mason's Trichrome (Sigma-Aldrich, St. Louis, MO) to visualize collagen deposition. Deparaffinized sections were immunoprobed for the expression of Platelet Endothelial Cell Adhesion Molecule-1 (PECAM-1) also known as cluster of differentiation 31(CD31) and alpha smooth muscle actin (α-SMA). Heat-induced antigen retrieval was performed in 10 mM citrate buffer, pH 6.0 for 20 min using a vegetable steamer. Sections were washed 3× for 2 min in PBS with 0.1% v/v Tween-20 (PBST). Endogenous peroxidase activity was blocked by incubation with 3% (v/v) hydrogen peroxide in methanol for 20 min at room temperature and sections were washed 3× for 2 min in PBST. Non-specific protein binding was blocked with 2.5% horse serum (Vector Labs, Burlingame, CA) for 20 min at room temperature. Samples were incubated with polyclonal anti-CD31 antibody (1:10 dilution) (ab28364, AbCam, Cambridge, England) or polyclonal anti-α-SMA antibody (1:300 dilution) (ab5694, AbCam, Cambridge, England) for 1h at room temperature, followed by washing 3× for 2 min in PBST and incubation with ImmPress Anti-Rabbit Ig (peroxidase) polymer detection kit (Vector Labs, Burlingame, CA) for 30 min. Sections were washed 3×2 min in PBST and color developed with DAB substrate kit for peroxidase (Vector Labs, Burlingame, CA) for 10 min at room temperature. Sections were rinsed in tap water, counterstained with

hematoxylin (Sigma-Aldrich, St. Louis, MO) and embedded in DPX mountant for Microscopy-10 (Electron Microscopy Sciences, Hatfield, PA).

Cell infiltration was quantified from three images of H&E stained sections (4× magnification) per scaffold for total of nine scaffolds per condition (unchanneled, 254 μm and 508 μm channel diameter). Outlines were drawn around cellular areas of each section using the 'free hand selection tool' in Image J (National Institutes of Health) and total cellular area determined. Area of cell infiltration (%) was calculated as (total cellular area/ total section area)*100.

Statistical Analyses

Data are expressed as mean ± standard deviation (SD). Statistically significant differences were determined by one- or two-way analysis of variance (ANOVA) and Bonferroni post-test. Statistical significance was accepted at $p<0.05$ and indicated in the figures as *$p<0.05$, **$p<0.01$ and ***$p<0.001$.

Supplementary Material

Refer to Web version on PubMed Central for supplementary material.

Acknowledgments

Jelena Rnjak-Kovacina and Lindsay S Wray contributed equally to this work. We thank the NIH (NIH P41 EB002520; EY020856) and the National Science Foundation Graduate Research Fellowship Program (NSF DGE 0806676) for support. We are grateful to Dr. Bruce Paniliatis for assistance with animal surgeries.

References

1. Laschke MW, Harder Y, Amon M, Martin I, Farhadi J, Ring A, Torio-Padron N, Schramm R, Rucker M, Junker D, Haufel JM, Carvalho C, Heberer M, Germann G, Vollmar B, Menger MD. Tissue Eng. 2006; 12:2093. [PubMed: 16968151]
2. Lokmic Z, Mitchell GM. Tissue Eng Part B Rev. 2008; 14:87. [PubMed: 18454636]
3. Lovett M, Lee K, Edwards A, Kaplan DL. Tissue Eng Part B Rev. 2009; 15:353. [PubMed: 19496677]
4. Phelps EA, Garcia AJ. Regen Med. 2009; 4:65. [PubMed: 19105617]
5. Rouwkema J, Rivron NC, Van Blitterswijk CA. Trends Biotechnol. 2008; 26:434. [PubMed: 18585808]
6. Du YA, Ghodousi M, Qi H, Haas N, Xiao WQ, Khademhosseini A. Biotechnol Bioeng. 2011; 108:1693. [PubMed: 21337336]
7. Golden AP, Tien J. Lab Chip. 2007; 7:720. [PubMed: 17538713]
8. Maidhof R, Marsano A, Lee EJ, Vunjak-Novakovic G. Biotechnol Prog. 2010; 26:565. [PubMed: 20052737]
9. Miller JS, Stevens KR, Yang MT, Baker BM, Nguyen DH, Cohen DM, Toro E, Chen AA, Galie PA, Yu X, Chaturvedi R, Bhatia SN, Chen CS. Nat Mater. 2012; 11:768. [PubMed: 22751181]
10. Radisic M, Park H, Chen F, Salazar-Lazzaro JE, Wang Y, Dennis R, Langer R, Freed LE, Vunjak-Novakovic G. Tissue Eng. 2006; 12:2077. [PubMed: 16968150]
11. Wray LS, Rnjak-Kovacina J, Mandal BB, Schmidt DF, Gil ES, Kaplan DL. Biomaterials. 2012; 33:9214. [PubMed: 23036961]
12. King KR, Wang CCJ, Kaazempur-Mofrad MR, Vacanti JP, Borenstein JT. Adv Mater. 2004; 16:2007.

13. Baranski JD, Chaturvedi RR, Stevens KR, Eyckmans J, Carvalho B, Solorzano RD, Yang MT, Miller JS, Bhatia SN, Chen CS. Proc Natl Acad Sci U S A. 2013; 110:7586. [PubMed: 23610423]
14. Shin M, Matsuda K, Ishii O, Terai H, Kaazempur-Mofrad M, Borenstein J, Detmar M, Vacanti JP. Biomed Microdevices. 2004; 6:269. [PubMed: 15548874]
15. Bagnaninchi PO, Yang Y, Zghoul N, Maffulli N, Wang RK, Haj AJ. Tissue Eng. 2007; 13:323. [PubMed: 17518566]
16. Moore MJ, Friedman JA, Lewellyn EB, Mantila SM, Krych AJ, Ameenuddin S, Knight AM, Lu L, Currier BL, Spinner RJ, Marsh RW, Windebank AJ, Yaszemski MJ. Biomaterials. 2006; 27:419. [PubMed: 16137759]
17. Nazhat SN, Neel EA, Kidane A, Ahmed I, Hope C, Kershaw M, Lee PD, Stride E, Saffari N, Knowles JC, Brown RA. Biomacromolecules. 2007; 8:543. [PubMed: 17291078]
18. Yu TT, Shoichet MS. Biomaterials. 2005; 26:1507. [PubMed: 15522752]
19. Pritchard EM, Kaplan DL. Expert Opin Drug Deliv. 2011; 8:797. [PubMed: 21453189]
20. Lichtenfels R, Biddison WE, Schulz H, Vogt AB, Martin R. J Immunol Methods. 1994; 172:227. [PubMed: 7518485]
21. Chen X, Aledia AS, Popson SA, Him L, Hughes CC, George SC. Tissue Eng Part A. 2010; 16:585. [PubMed: 19737050]
22. Koike N, Fukumura D, Gralla O, Au P, Schechner JS, Jain RK. Nature. 2004; 428:138. [PubMed: 15014486]
23. Levenberg S, Rouwkema J, Macdonald M, Garfein ES, Kohane DS, Darland DC, Marini R, Van Blitterswijk CA, Mulligan RC, D'amore PA, Langer R. Nat Biotechnol. 2005; 23:879. [PubMed: 15965465]
24. Hu X, Shmelev K, Sun L, Gil ES, Park SH, Cebe P, Kaplan DL. Biomacromolecules. 2011; 12:1686. [PubMed: 21425769]
25. Horan RL, Antle K, Collette AL, Wang Y, Huang J, Moreau JE, Volloch V, Kaplan DL, Altman GH. Biomaterials. 2005; 26:3385. [PubMed: 15621227]
26. Wang Y, Rudym DD, Walsh A, Abrahamsen L, Kim HJ, Kim HS, Kirker-Head C, Kaplan DL. Biomaterials. 2008; 29:3415. [PubMed: 18502501]
27. Lovett M, Cannizzaro C, Daheron L, Messmer B, Vunjak-Novakovic G, Kaplan DL. Biomaterials. 2007; 28:5271. [PubMed: 17727944]
28. Lovett M, Eng G, Kluge JA, Cannizzaro C, Vunjak-Novakovic G, Kaplan DL. Organogenesis. 2010; 6:217. [PubMed: 21220960]
29. Bellas E, Marra KG, Kaplan DL. Tissue Eng Part C Methods. 2013
30. Zhang W, Wang X, Wang S, Zhao J, Xu L, Zhu C, Zeng D, Chen J, Zhang Z, Kaplan DL, Jiang X. Biomaterials. 2011; 32:9415. [PubMed: 21889205]
31. Rockwood DN, Preda RC, Yucel T, Wang X, Lovett ML, Kaplan DL. Nat Protoc. 2011; 6:1612. [PubMed: 21959241]
32. Subramanian B, Rudym D, Cannizzaro C, Perrone R, Zhou J, Kaplan DL. Tissue Eng Part A. 2010; 16:2821. [PubMed: 20486787]
33. Lovett M, Rockwood D, Baryshyan A, Kaplan DL. Tissue Eng Part C Methods. 2010; 16:1565. [PubMed: 20528664]

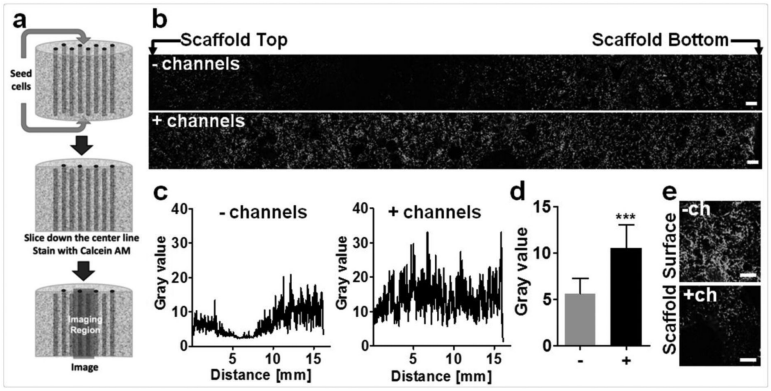

Figure 1.

Cell infiltration *in vitro*. (a) Scaffolds (h= 15 mm; ø= 12 mm) were seeded with 8×10^6 of human dermal fibroblasts, incubated for 24 hours, sliced down the center line along the axis of the hollow channels, and stained with calcein AM. (b) Representative fluorescent images along the middle of the unchanneled and channeled scaffold. Scale bars = 300 μm. (c) Representative cell infiltration analysis, which shows lower pixel grey value along the length of the unchanneled scaffold compared to the channeled scaffold. (d) Average pixel value for unchanneled (−) and channeled (+) scaffolds. There was higher calcein AM staining in channeled scaffold compared to the unchanneled scaffold (±SD, ***$p<0.001$, n=4). (e) Representative images of unchanneled (−) and channeled (+) scaffold surfaces stained with calcein AM. Scale bar= 300 μm.

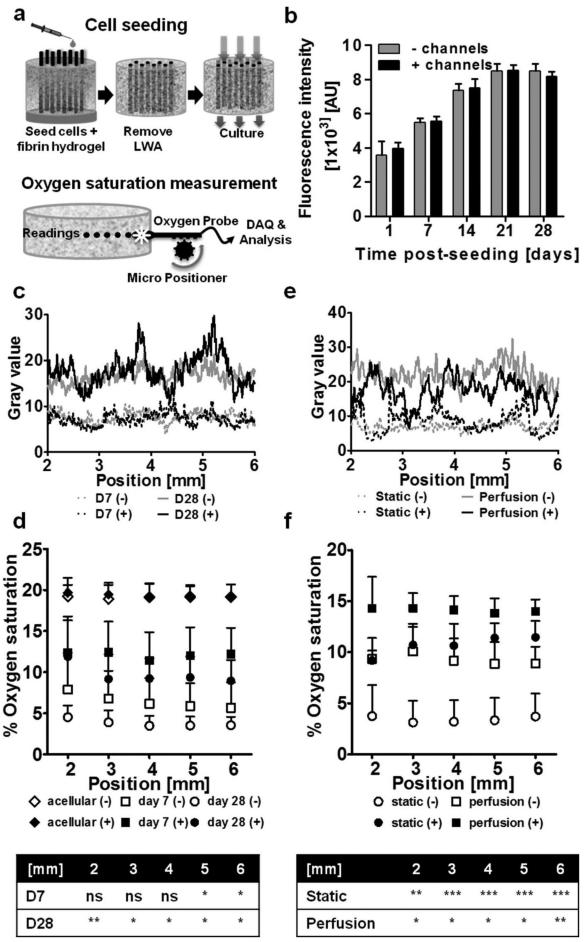

[mm]	2	3	4	5	6
D7	ns	ns	ns	*	*
D28	**	*	*	*	*

[mm]	2	3	4	5	6
Static	**	***	***	***	***
Perfusion	*	*	*	*	**

Figure 2.

Oxygen distribution within porous scaffolds seeded with human dermal fibroblasts. (a) Schematic of cell seeding and oxygen probing device and measurement set-up. (b) Dermal fibroblasts cultured in unchanneled and channeled scaffolds over the course of 28 days were measured for metabolic activity using the Alamar Blue assay. At each time point there was no difference in metabolic activity between the unchanneled and channeled scaffolds (± SD; n=3). (c) Cell distribution in channeled and unchanneled scaffolds between 2 and 6 mm along the scaffold centerline (where oxygen saturation measurements were made) at day 7 and day 28 as determined by pixel analysis from calcein AM stained images. (d) Oxygen saturation along the scaffold centerline at day 7 and 28. The table indicates statistically significant differences in oxygen saturation between unchanneled and channeled constructs at day 7 and day 28 (± SD; *p<0.05, **p<0.01; n=3). (e) Cell distribution (day 7) between 2 and 6 mm along the scaffold centerline (where oxygen saturation measurements were made) in channeled and unchanneled scaffolds cultured under static or perfusion conditions as determined by pixel analysis from calcein AM stained images. (f) Oxygen saturation along the scaffold centerline at day 7 in scaffolds cultured statically or with perfusion. The table indicates statistically significant differences in oxygen saturation between unchanneled and channeled constructs in the static and perfusion system (± SD; *p<0.05, **p<0.01, ***p<0.001; n=3).

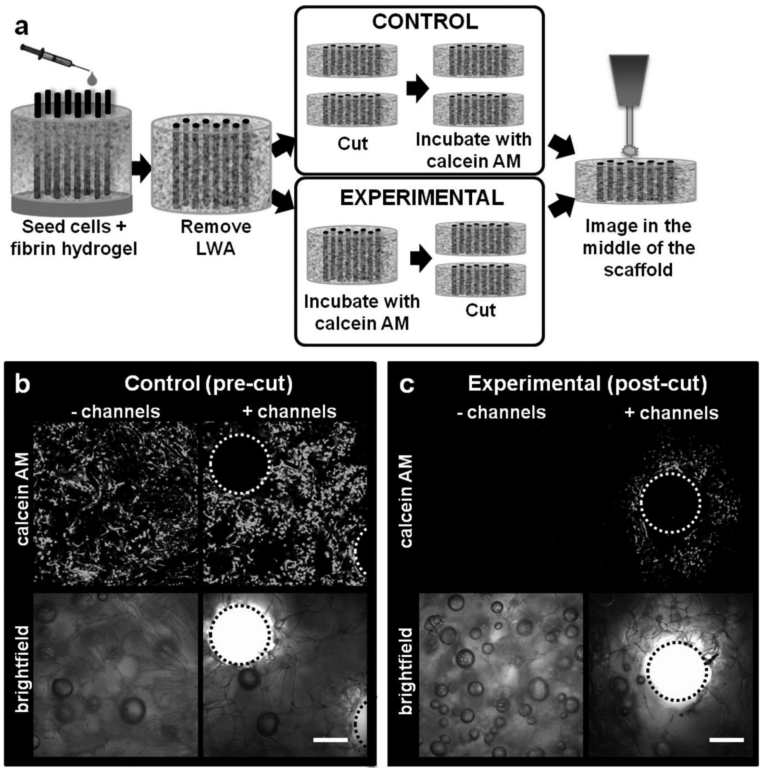

Figure 3.

Diffusion of calcein AM into the scaffold bulk. (a) Unchanneled and channeled scaffolds (height=6 mm, ø=12 mm) were seeded with human dermal fibroblasts and cultured statically. One group of scaffolds was cut down the centerline and stained with calcein AM (control, pre-cut). Another group was not sliced down the centerline prior to staining with calcein AM and therefore any positive staining in the experimental condition resulted from diffusion of the calcein AM molecule into the bulk of the scaffold (experimental, post-cut). (b) Representative control samples showing presence of live cells in the middle of unchanneled and channeled scaffold. (c) Representative experimental samples showing calcein AM diffusion into the middle of channeled, but not unchanneled scaffolds. Average radius of calcein AM diffusion around the channels as determined by Image J analysis was 321.7±13.5 μm. Scale bars=300 μm.

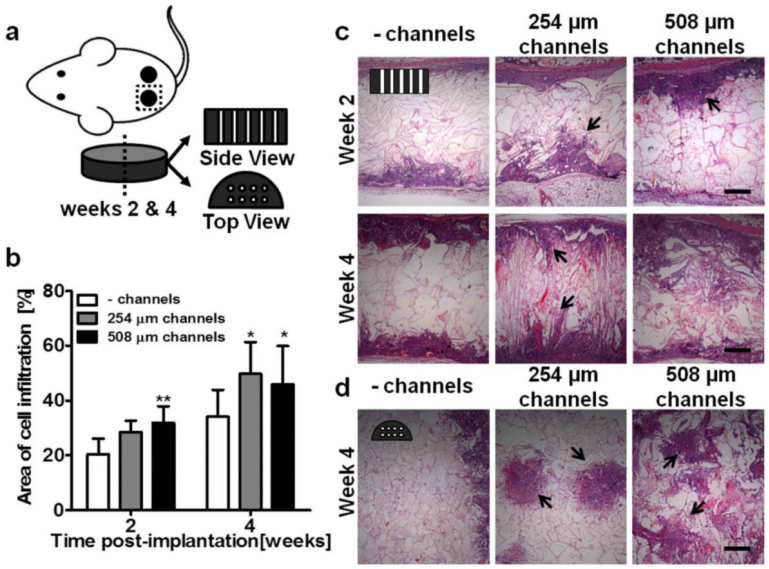

Figure 4.

In vivo cell and tissue infiltration into unchanneled and channeled scaffolds. (a) Schematic of experimental setup. Scaffolds were 8 mm in diameter and 2 mm in height. Channeled scaffold contained either 254 µm diameter or 508 µm diameter channels. Scaffolds were explanted after 2 and 4 weeks and histologically visualized in two configurations; 'side view' slices show the length of the channels and 'top view' slices show the circular cross-section of the channels. (b) The area of cell infiltration was analyzed and quantified from H&E stained images (± SD; *$p<0.05$, **$p<0.01$; n=9). (c) In the 'side view' (H&E), minimal cell infiltration was observed in the unchanneled scaffolds while in the 254 µm and 508 µm diameter scaffolds, cells were present within the scaffold. At week 2, the location of the channels was visible (indicated by black arrows) while in weeks 4, channel location was less visible in the 508 µm scaffolds but still roughly visible in the 254 µm scaffolds. (d) In the 'top view', the unchanneled scaffolds showed minimal cell infiltration while cell infiltration is clearly visible in the 254 µm and 508 µm diameter channeled scaffolds. In the 254 µm scaffolds the infiltration was roughly confined to the channels while in the 508 µm scaffolds, cell infiltration was less confined to the channel.

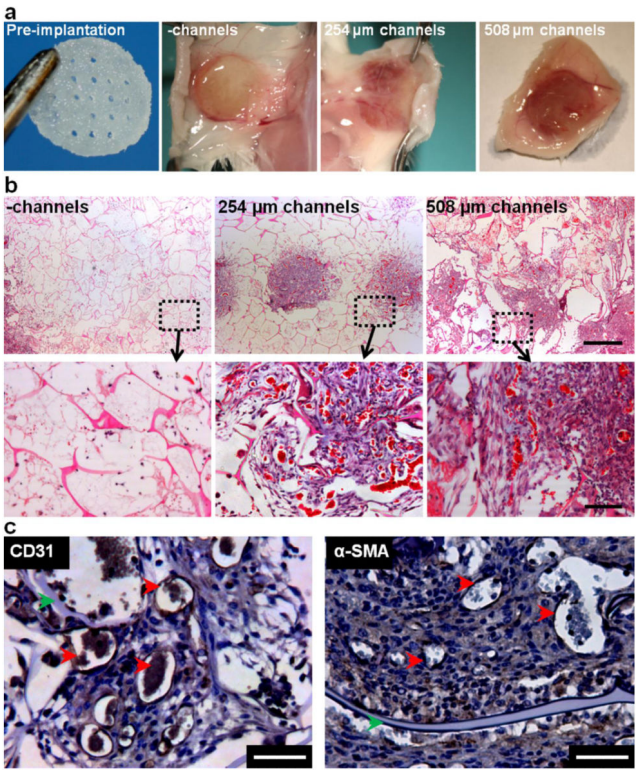

Figure 5.

In vivo remodeling and vascularization of subcutaneously implanted unchanneled and channeled scaffolds. (a) Visual inspection of explanted scaffolds showed that the channeled scaffolds were highly vascularized. (b) Masson's trichrome staining shows perfused blood vessels (bright red) and scaffold remodeling (collagen deposition stained blue). Scale bar=500 μm in the first row and 100 μm in the second row. (c) Lumen structures stain positively for CD31 and α-SMA indicating that the vessels are endothelialized and mature (red arrows). After four weeks of implantation the silk scaffold is still visible (green arrows). Scale bar=50 μm.

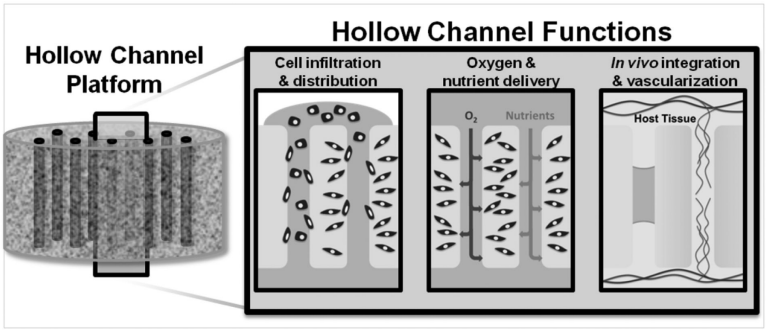

Figure 6.

The hollow channel platform is advantageous for engineering tissue constructs *in vitro* and *in vivo*. Hollow channel platforms enhance cell infiltration into the bulk of the scaffold during seeding. During culture, the channels improve delivery of oxygen and nutrients. The channels direct *in vitro* prevascularization and improve *in vivo* host tissue integration and vascularization.